

RESEARCH ARTICLE

The use of variable delay multipulse chemical exchange saturation transfer for separately assessing different CEST pools in the human brain at 7T

Bárbara Schmitz-Abecassis¹  | Elena Vinogradov^{2,3}  | Jannie P. Wijnen⁴  |
Thijs van Harten¹  | Evita C. Wiegers⁴  | Hans Hoogduin⁴  |
Matthias J. P. van Osch¹  | Ece Ercan¹  

¹C.J. Gorter Center for High Field MRI, Department of Radiology, Leiden University Medical Center, Leiden, The Netherlands

²Department of Radiology, UT Southwestern Medical Center, Dallas, Texas, USA

³Advanced Imaging Research Center, UT Southwestern Medical Center, Dallas, Texas, USA

⁴Imaging Division, University Medical Center Utrecht, Utrecht, The Netherlands

Correspondence

Ece Ercan, C.J. Gorter Center for High Field MRI, Department of Radiology, C3Q, Leiden University Medical Center, P.O. Box 9600, 2300 RC, Leiden, The Netherlands.

Email: a.e.ercan@lumc.nl

Funding information

The Dutch Research Council (NWO) Talent Programme Veni project number 16862 and the Medical Delta Cancer Diagnostics 3.0

Purpose: Current challenges of *in vivo* CEST imaging include overlapping signals from different pools. The overlap arises from closely resonating pools and/or the broad magnetization transfer contrast (MTC) from macromolecules. This study aimed to evaluate the feasibility of variable delay multipulse (VDMP) CEST to separately assess solute pools with different chemical exchange rates in the human brain *in vivo*, while mitigating the MTC.

Methods: VDMP saturation buildup curves were simulated for amines, amides, and relayed nuclear Overhauser effect. VDMP data were acquired from glutamate and bovine serum albumin phantoms, and from six healthy volunteers at 7T. For the *in vivo* data, MTC removal was performed via a three-pool Lorentzian fitting. Different B_1 amplitudes and mixing times were used to evaluate CEST pools with different exchange rates.

Results: The results show the importance of removing MTC when applying VDMP *in vivo* and the influence of B_1 for distinguishing different pools. Finally, the optimal B_1 and mixing times to effectively saturate slow- and fast-exchanging components are also reported. Slow-exchanging amides and rNOE components could be distinguished when using $B_1 = 1 \mu\text{T}$ and $t_{\text{mix}} = 10 \text{ ms}$ and 40 ms , respectively. Fast-exchanging components reached the highest saturation when using a $B_1 = 2.8 \mu\text{T}$ and $t_{\text{mix}} = 0 \text{ ms}$.

Conclusion: VDMP is a powerful CEST-editing tool, exploiting chemical exchange-rate differences. After MTC removal, it allows separate assessment of slow- and fast-exchanging solute pools in *in vivo* human brain.

This is an open access article under the terms of the Creative Commons Attribution-NonCommercial License, which permits use, distribution and reproduction in any medium, provided the original work is properly cited and is not used for commercial purposes.

© 2021 The Authors. *Magnetic Resonance in Medicine* published by Wiley Periodicals LLC on behalf of International Society for Magnetic Resonance in Medicine

KEYWORDS

7T, chemical exchange saturation transfer (CEST), ultrahigh field, variable delay multipulse (VDMP)-CEST

1 | INTRODUCTION

CEST has received increased attention in recent years given its ability to noninvasively image solutes such as proteins, peptides, and metabolites *in vivo*.^{1,2} Even with advantages as high spatial resolution and SNR, a crucial challenge of CEST is the quantification of CEST effects from different solutes in the human brain. This is mainly caused by an overlapping signal from different pools (eg, amide protons and amines, as well as the broad magnetization transfer contrast [MTC] effect), resulting in a lack of specificity to differentiate the CEST effect from different pools.³ Exploiting the differences in the exchange rates and using high or low B_1 amplitude to target a specific CEST pool of interest could improve the specificity in the observation of a certain CEST pool.³ However, the use of higher B_1 amplitudes results in a more-pronounced MT effect and more direct saturation of water; thus it creates a stronger overlap with the semisolid macromolecular pool. Magnetization transfer ratio asymmetry analysis, a quantification method based on the subtraction of signals obtained with positive and negative offset with respect to the water frequency, has been widely used for eliminating MTC and quantifying the CEST effect from the solute pool of interest.^{4,5} Nevertheless, the lack of symmetry in the MT effect and the pronounced relayed nuclear Overhauser effect (rNOE) at 7T complicate the use of magnetization transfer ratio asymmetry analysis, especially at higher field strengths.

A relatively novel CEST method called variable-delay multipulse CEST (VDMP-CEST), was introduced to address this challenge.⁶ VDMP-CEST uses the interpulse delay (mixing times) of the pulsed CEST sequences as an exchange filter to exploit exchange-rate differences of different CEST pools. Varying the mixing time allows the observation of differences in the saturation buildup depending on the intrinsic exchange-rate properties of the solute pool of interest. For instance, amines, such as glutamate (Glu) and creatine, are fast-exchanging molecules with exchange rates of 700 Hz and higher, whereas amide and rNOE effects can originate from slow-exchanging molecules with exchange rates of 10 to 30 Hz.^{7,8} Amide effects with higher exchange rates (eg, 162 Hz and 365 Hz), but still lower than those of amines, were also reported in the literature.⁹ Because of the difference in the exchange rate, it will take a longer time for the saturation to build-up for amides compared with amines. This is reflected in the buildup curves that show the change in Z magnetization as a function of mixing time. Therefore, amines are expected

to have a rather quick saturation buildup profile compared with that of rNOE and amide pools, which would require a longer time to build-up saturation.

To date, all VDMP-CEST applications but one were performed on phantoms and in *in vivo* mouse models.^{5,10,11} Only one study showed the feasibility of VDMP-CEST in the human brain.⁵ In this study, only one B_1 amplitude was used and the buildup curves from different CEST pools in the human brain were not investigated. The use of different B_1 amplitudes, in addition to changing the mixing times, could further help separately evaluate the CEST effect from various CEST pools in the human brain. Moreover, VDMP does not account for MTC from macromolecules, hindering an accurate quantification of the CEST effect. A previous study used subtraction of two different mixing times to suppress MTC in the human brain white matter (WM).⁵ Because MTC varies in different tissue types, it is difficult to eliminate MTC in all brain regions through subtraction.¹² Moreover, the use of different B_1 amplitudes will result in different levels of MTC contribution, and thus requires a more sophisticated method than subtraction to eliminate the MTC.

In this study, we aimed to evaluate the potential utility of VDMP-CEST for exchange-rate sensitive imaging and thereby to separately assess CEST effects from amide, amine, and rNOE pools. Our secondary goal was to evaluate VDMP-CEST in combination with MTC removal in *in vivo* human brain. These aims are achieved by simulations, phantom scans, and *in vivo* experiments of the human brain. First, we simulated the VDMP buildup curves of amide, amine, and rNOE pools. Second, for confirmation of the VDMP effects in the case of two pools, we used phantom experiments. Finally, we applied VDMP-CEST in the human brain at 7T using various B_1 amplitudes and removing the MTC via a three-pool Lorentzian model. We generated VDMP buildup curves from amide, amine, and rNOE pools after the MTC removal and investigated the evolution of VDMP buildup curves from these pools for different B_1 amplitudes.

2 | METHODS

2.1 | Simulations

VDMP saturation buildup curves from CEST pools with different exchange rates in the human brain were simulated similar to that in a previous study.¹¹ A two-pool model (water + one solute pool) was used to simulate two conditions: slow exchange and fast exchange. For slow-exchanging

TABLE 1 Image acquisition parameters represented for both phantom and *in vivo* experiments

Imaging parameters	Phantom VDMP-CEST	In vivo VDMP-CEST	3D T ₁ -weighted images	DREAM for B ₁ map
TR/TE/TI, ms	3.7/2	3.7/2	4.2/1.85/1300	8.0/1.97
FA, degrees	5	5	7	10
FOV, mm ³	246 × 246 × 21	246 × 246 × 21	246 × 246 × 246	246 × 246 × 21
Voxel size, mm ³	1.5 × 1.5 × 3	1.5 × 1.5 × 3	0.9 × 0.9 × 0.9	1.5 × 1.5 × 1.5
TFE factor	75	75	352	164
SENSE factor (RL/AP/FH)	2/1/1	2/1/1	2.5/2/1	–
B ₁ amplitude	2 μT & 3 μT	0.99 μT, 1.99 μT, 2.81 μT, 3.26 μT	–	–
Mixing times, ms	0, 10, 20, 40, 60, 80, 100	0, 10, 15, 20, 40, 60, 100	–	–
Total scan time, min	~42 min per B ₁	~40 min per B ₁	02:21 min	00:09 min

Abbreviations: AP, anterior-posterior; FA, flip angle; FH, foot-head; RL, right-left; TFE, turbo field echo; VDMP, variable delay multipulse.

molecules, two cases were considered: amides (frequency offset $[\Delta] = 3.5$ ppm, exchange rate $[k_{sw}] = 30$ Hz) and rNOE ($\Delta = -3.5$ ppm, $k_{sw} = 16$ Hz). To represent fast-exchanging molecules, amines (Glu, $\Delta = 3$ ppm, $k_{sw} = 5500$ Hz) were simulated. Additionally, a three-pool model (water + two solute pools) was employed to simulate the overlap of amide and amine pools at 3 ppm (amide + amine). The details on simulations can be found in the Supporting Information.

2.2 | Phantom preparation

One phantom consisting of three vials of 60 mL was prepared and assembled into one glass recipient filled with fomblin. To mimic the amine and amide proton exchangeable groups separately and in combination, the vials contained (1) a 50 mM solution of Glu, (2) 10% bovine serum albumin (BSA), and (3) a mixture solution of 10% BSA and 50 mM Glu. Details of phantom preparation are explained in the Supporting Information.

2.3 | Human subjects

Six healthy female volunteers (Mean age: 28 years; SD = 4) were included in the study. Written informed consent was obtained from the volunteers. The study adhered to the local institutional review board guidelines and approval.

2.4 | MRI scans

MRI acquisitions were performed on a whole-body 7T Achieva Philips MRI scanner (Philips Healthcare) equipped with a dual-transmit and a 32-channel receiver head coil (Nova Medical Inc.).

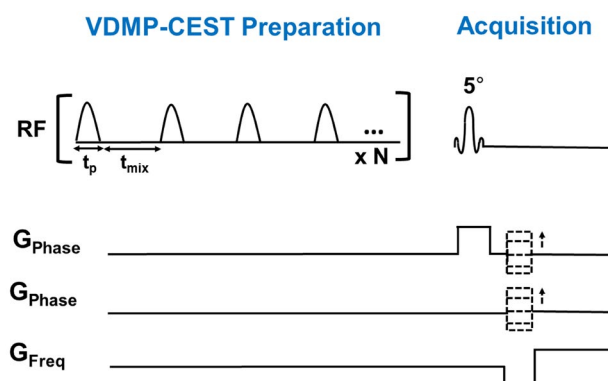


FIGURE 1 VDMP pulse sequence preparation, where the mixing time (t_{mix}) is illustrated as the interpulse delay. The total preparation time will also depend on the pulse duration (t_p) and the number of RF pulses (N). VDMP-CEST, variable delay multipulse chemical-exchange saturation transfer

The scan protocol for the phantom and *in vivo* acquisitions consisted of a short survey scan, a SENSE reference scan, acquisition of a B₀ map to be used to perform third-order B₀ shimming, acquisition of a B₁ map using the dual refocusing echo acquisition mode (DREAM) sequence,¹³ and VDMP-CEST scans. The B₁ maps for each volunteer can be found in Supporting Information Figure S1. For *in vivo* scans, a MPRAGE sequence was additionally used to obtain 3D T₁-weighted images to assess gray matter (GM) and WM tissue probabilities per voxel. Imaging parameters can be found in Table 1.

For VDMP-CEST scans, a pulsed 3D CEST preparation was followed by a gradient echo readout with FLASH. Shim parameters obtained by third-order shimming were used to improve B₀ inhomogeneities. CEST preparation employed 20 sinc-Gauss pulses of 20 ms duration. The VDMP-CEST pulse sequence is illustrated in Figure 1. A

total of 29 frequencies with a step size of 107 Hz were acquired between -1500 and 1500 Hz. For normalization, an M_0 image was acquired at $500,000$ Hz (around 1678 ppm). Seven mixing times (t_{mix}) were used ($0, 10, 15, 20, 40, 60, 100$ ms). For phantom scans, two different B_1 amplitudes were used: $2 \mu\text{T}$ and $3 \mu\text{T}$. For *in vivo* scans, four different B_1 amplitudes were used (one per subject): $0.99 \mu\text{T}$, $1.99 \mu\text{T}$, $2.81 \mu\text{T}$, and $3.26 \mu\text{T}$. The B_1 amplitudes used and the corresponding B_1 average power for each mixing time are listed in Supporting Information Table S1. B_1 average power was defined as $B_{1 \text{ avg power}} = \sqrt{\frac{1}{PTR} \int_0^{PTR} B_1^2 dt}$, where B_1 is the B_1 amplitude of the pulse and pulse repetition time (PTR) is the sum of the pulse widths (t_p) and interpulse delays (t_{mix}), $PTR = t_p + t_{\text{mix}}$.¹⁴

To investigate the role of B_1 average power during the whole saturation duration on the buildup curves, VDMP-CEST experiment was conducted on a fifth volunteer, while keeping a fixed B_1 average power ($1.55 \mu\text{T}$) and using the previously listed mixing times. To keep the B_1 average power the same for all mixing times, the B_1 amplitude was increased while increasing the t_{mix} .

To investigate the reliability of Lorentzian-fitting parameters, a sixth volunteer was scanned with a CEST sequence with B_1 amplitude of $0.99 \mu\text{T}$, t_{mix} of 10 ms, and a larger frequency span between $-75,000$ and $75,000$ Hz. More information on this acquisition is described in the Supporting Information.

2.5 | Image processing of the *in vivo* data

Probability maps of the GM and WM were retrieved from the 3D T_1 -weighted image using FMRIB (Functional Magnetic Resonance Imaging of the Brain) Software Library (FSL) v6.0.¹⁵ Segmentations were performed on the original 3D T_1 -weighted image. For this purpose, the skull was removed using the Brain Extraction Tool (BET) in FSL.¹⁶ Extracted brain images were segmented using fMRIB's automated segmentation tool (FAST).¹⁷ The spatial volume estimation maps were registered to the CEST space using a resampler contained in the FreeSurfer package.¹⁸ A voxel was regarded as GM or WM if the partial volume estimation exceeded the threshold of 0.7 .

2.6 | Data analysis

Custom-written MATLAB scripts were used for data analysis. Corrections for B_0 field inhomogeneities were performed by spline interpolation followed by shifting of the Z -spectra based on the minimum Z determination. The reference scan acquired at a far offset (M_0 image) was

used to normalize all CEST images. ROI-based assessment of the Z magnetization was done for both phantom and *in vivo* data over the frequency ranges by calculating the average of all voxels.

For the phantom data, ROIs were manually drawn on each vial on the midslice (Supporting Information Figure S2) and VDMP saturation buildup curves for different pools were calculated for each ROI for all mixing times. For the human brain, the WM and GM buildup curves were evaluated within the midslice by masking the CEST data with the previously obtained GM and WM masks. For MT contrast removal in the *in vivo* data, $(1 - S/S_0)$ was calculated for each frequency of the Z -spectra from each mixing time. A three-pool Lorentzian model was fitted for each t_{mix} using the Levenberg–Marquardt algorithm.¹⁹ The model used consisted of water, MT, and rNOE pools at fixed chemical shift values (0 ppm, 0 ppm, -3.5 ppm, respectively). The initial point for the MT pool amplitude was defined as the signal amplitude of $(1 - S/S_0)$ at 5 ppm. The initial points, upper and lower boundaries of all fit parameters, are listed in the Supporting Information Table S2. The fitted MT pool was subsequently removed (subtracted) from $(1 - S/S_0)$. The MT-removed Z -spectra were used to assess the CEST signal at the frequency of interest (3.5 ppm for amides, 2 ppm for amines, and -3.5 ppm for rNOE) for each mixing time. VDMP saturation buildup curves were generated as a function of the ratio between the change in saturation ($S - S_0$) and S_0 , for all the mixing times (t_{mix}). The VDMP curves were then normalized to the first mixing time ($t_{\text{mix}} = 0$ ms). The image processing and analysis pipeline for the *in vivo* data are shown in Figure 2. Based on VDMP buildup curves, the optimal B_1 and mixing time combinations were determined for amide, amine, and rNOE pools.

Finally, voxel-based VDMP-CEST maps were generated by removing the MTC per voxel through the three-pool Lorentzian fittings as described above. The B_1 inhomogeneities were linearly corrected per voxel by using the B_1 map obtained from the same subject. The contrast of amide, amine, and rNOE pools was evaluated. The contrast observed corresponds to $(1 - S/S_0)$ after the MTC removal.

3 | RESULTS

3.1 | Simulations

Figure 3A shows the buildup curves that are simulated for amides, rNOE, and amines (Glu) using a two-pool model. Slow-exchanging pools (amides and rNOE) show a gradual saturation buildup, whereas a fast decay without a buildup is observed for the fast-exchanging amines. In Figure 3B, the buildup curve for the mixture of amide and amines

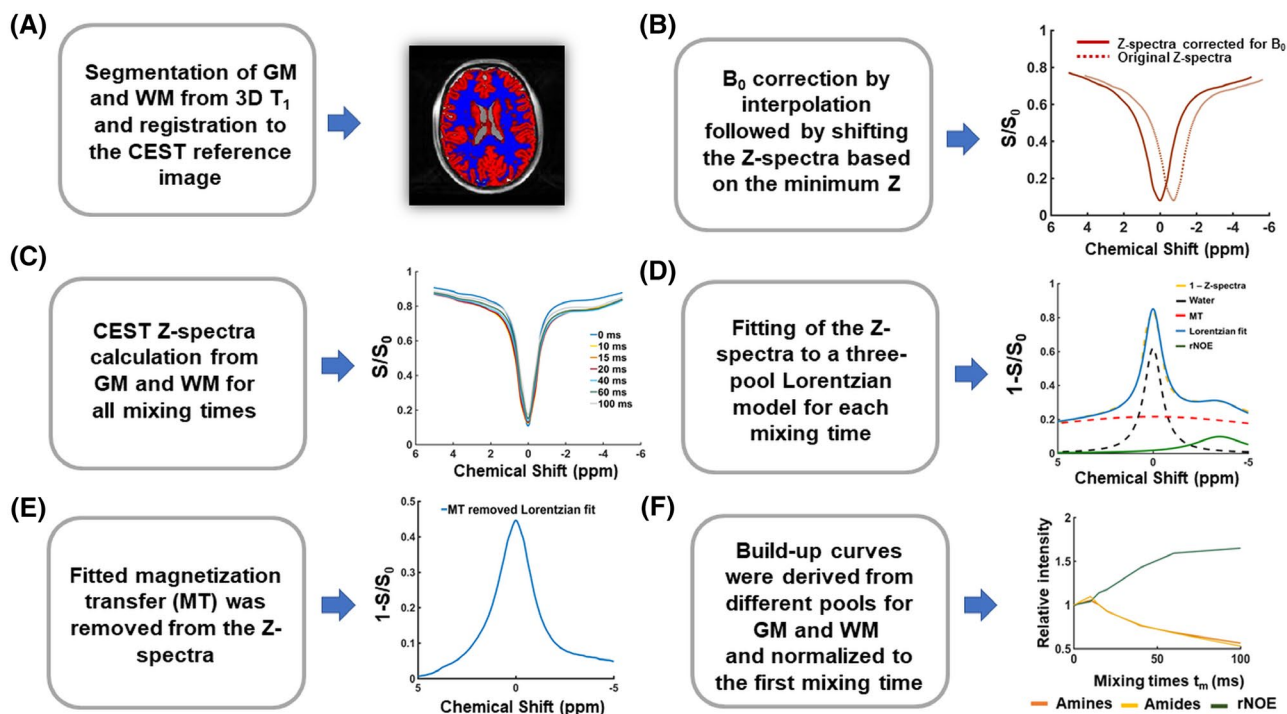


FIGURE 2 Image processing and analysis. A, Gray matter (GM) and white matter (WM) were segmented from the 3D T_1 and registered to CEST space. B, B_0 field inhomogeneity corrections were performed by interpolation and shifting of the Z-spectra based on the minimum z. C, Z-spectra were plotted for each mixing time from the average signal taken from the voxels in the GM and WM. D, Z-spectra from all mixing times were fitted to a three-pool Lorentzian model for GM and WM. E, The MTC pool fitted in step (D) was subtracted from the Z-spectra. F, VDMP buildup curves were generated for GM and WM for each B_1 amplitude, and normalized to the first mixing time. rNOE, relayed nuclear Overhauser enhancement; VDMP, variable delay multipulse

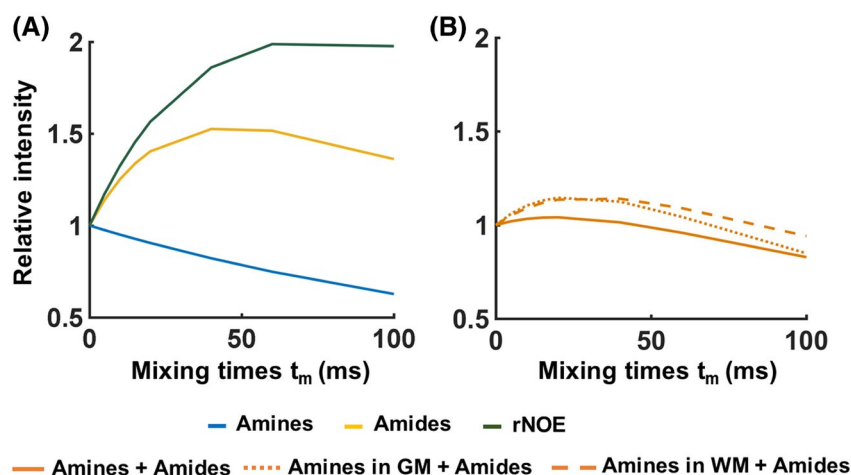


FIGURE 3 Simulated and normalized variable delay multipulse saturation buildup curves when (A) a two-pool (water + one solute) model was used for amine, amide, and nuclear Overhauser enhancement pools individually. In B, a three-pool model (water + amide + amine) was used to simulate the normalized buildup curves for a combination of amides and amines (1) when maintaining the same water T_1 value and solute pool fractions of amides and amines as those used in (A) (full orange line), and (2) when the combination included amine (glutamate) pool fractions and water T_1 values representative of the conditions found in the human brain gray (GM; dotted orange line) and white matter (WM; dashed orange line). rNOE, relayed nuclear Overhauser enhancement

(Glu) at 3 ppm, that is simulated using a three-pool model, is shown with the orange line. In this case, the buildup trend follows a similar trend to that from the amine-only

pool, suggesting that the very fast-exchanging nature of amines dominates the overall signal. In Figure 3B, a similar graph is also displayed for a mixture of amide and amine

(Glu) concentrations at 3 ppm using the Glu concentration in the human GM and WM. The dotted line represents the buildup curve of amines in the GM, where Glu concentrations are higher than in the WM.

3.2 | Phantom studies

Figure 4A illustrates the saturation buildup trend for the amide and rNOE pools in dotted and dashed lines, respectively, when a B_1 of $2 \mu\text{T}$ is used. Both in the mixture phantom as well as in the 10% BSA phantom, both amide and rNOE slow-exchanging pools exhibit a slow buildup of saturation. A similar trend is seen in Figure 4B for a B_1 of $3 \mu\text{T}$. Whereas from the fast-exchanging Glu pool, it is not possible to observe at which time point it reaches its saturation peak. Because the VDMP curves are normalized to the first mixing time, there is a continuous decrease in saturation across the mixing times as a result of T_1 relaxation.⁶ For a B_1 of $2 \mu\text{T}$ (Figure 4A), the signal from Glu (light-blue line) is not observable for $t_{\text{mix}} > 0$. However, a B_1 of $3 \mu\text{T}$ is sufficient to observe a more efficient saturation of Glu (Figure 4B). For both cases, the mixture phantom follows the same buildup trend at 3 ppm (dark-blue solid line) and at 3.5 ppm (yellow dotted line), similar to the trend of amides from a BSA-only phantom (green dotted line).

3.3 | Human studies

In Figure 5A,B, the Z-spectra obtained using a B_1 of $0.99 \mu\text{T}$ are shown for all t_{mix} from the GM and WM, respectively.

When using a lower B_1 , a more evident rNOE contrast is observed at -3.5 ppm. This holds especially in the WM (Figure 5B). Independently of the mixing times, a broadening of the Z-spectra is observed with a higher B_1 value ($B_1 = 3.26 \mu\text{T}$). (Figure 5C,D), in line with a MTC increase at higher B_1 .²⁰ A trend of increased broadening with increasing B_1 was observed also for $B_1 = 1.99 \mu\text{T}$ and $B_1 = 2.81 \mu\text{T}$ (data not shown).

The presence of MTC in *in vivo* human brain is notorious in VDMP-CEST buildup curves because all CEST pools buildup trends are similar to the one of the MT when MT removal is not applied (Figure 6A). Upon removing the MTC, a gradual buildup trend was observed for the slow-exchanging molecules (rNOE and amides), whereas a faster decay could be observed for fast-exchanging ones (amines), similar to the simulation and phantom results (Figure 6B). A rNOE curve displays significantly different behavior than amide and amine pools, both in terms of buildup and the level-off, reflecting the slower and different (relayed) nature of the processes involved.

The reliability of Lorentzian fittings was investigated based on the acquisition with a larger frequency span. Histograms of the fitting parameters are shown in the Supporting Information Figure S3. Except for the full-width half-maximum (FWHM) of NOE, which was restricted by the upper boundary for some WM voxels, none of the fit parameters were restricted by fit borders when all frequencies were used. A discrepancy was observed between the larger frequency span and a smaller subset of 27 frequency offsets for FWHM of MT and amplitude of rNOE.

To investigate the influence of the B_1 on the saturation buildup trends of CEST pools in the human brain,

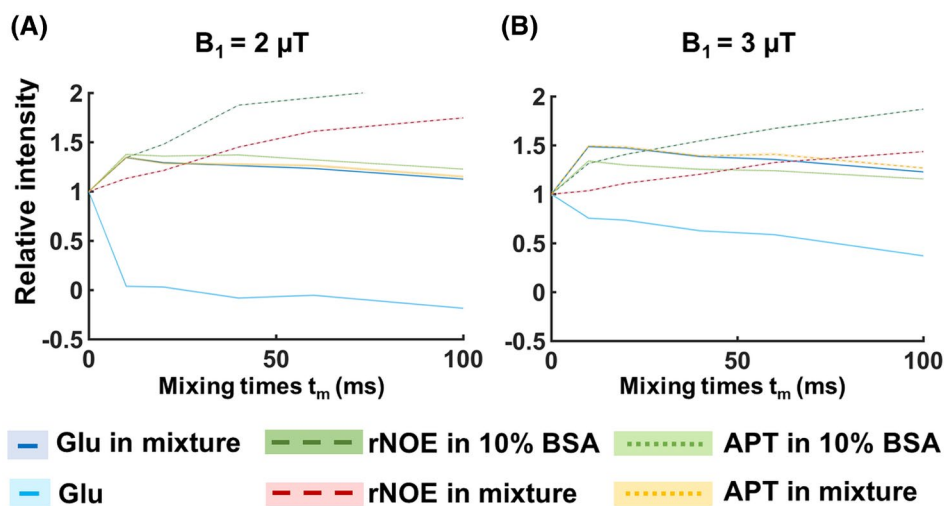


FIGURE 4 VDMP saturation buildup curves from the phantom experiment (normalized to the first t_{mix}). The mean signals from individual phantoms and from the mixture phantom are presented with separate lines. rNOE (dashed lines) and amide (dotted lines) are retrieved from the 10% BSA and mixture (50 mM glutamate and 10% BSA) phantom. Full light- and dark-blue lines represent glutamate from the single and mixture phantom, respectively. B_1 amplitude per pulse unit was $2 \mu\text{T}$ for (A) and $3 \mu\text{T}$ for (B). SD for each ROI is highlighted. APT, Amide proton transfer; BSA, bovine serum albumin; rNOE, relayed nuclear Overhauser enhancement; VDMP, variable delay multipulse

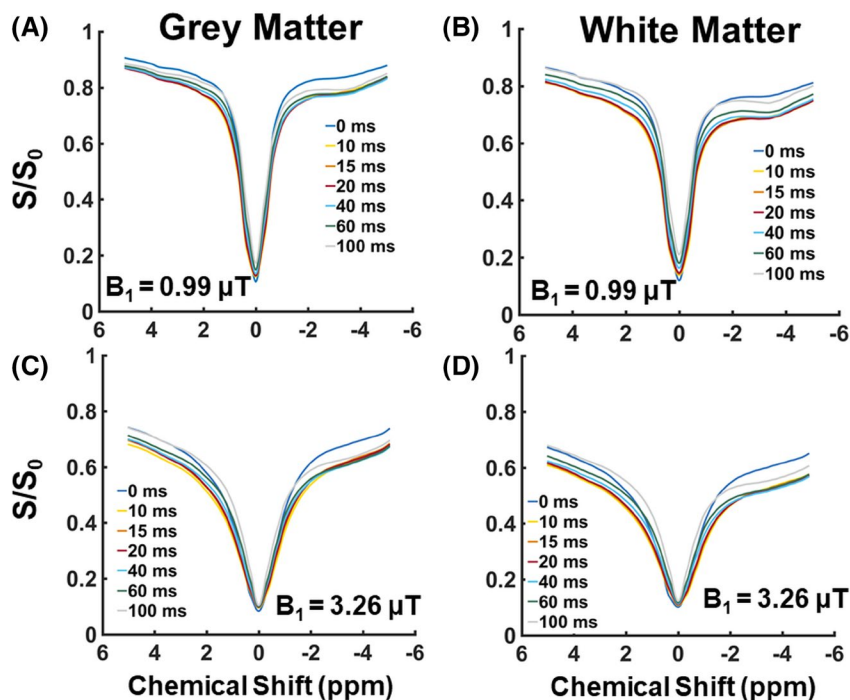


FIGURE 5 The B_0 -corrected Z-spectra from the gray matter and white matter for the different mixing times before removing the magnetization transfer contrast. In A and B, the Z-spectra are displayed when having applied a B_1 amplitude of $0.99 \mu\text{T}$. In C and D, the Z-spectra are shown when having adopted a higher B_1 amplitude of $3.26 \mu\text{T}$

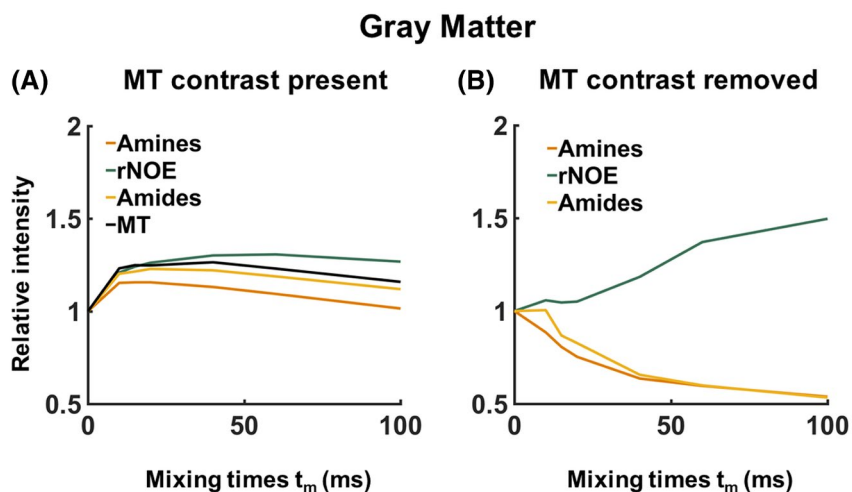


FIGURE 6 A typical example of the effect of magnetization transfer contrast (MTC) on the variable delay multipulse buildup curves from the human brain white matter for $B_1 = 3.26 \mu\text{T}$. In A, the saturation buildup of the different CEST pools is plotted together with the MTC. In B, the MTC has been removed, and the trend of the VDMP buildup curves from the CEST pools with different exchange rates can be distinguished. MT, magnetization transfer; rNOE, relayed nuclear Overhauser enhancement

MTC-removed VDMP build curves are plotted for different B_1 amplitudes (Figure 7, Supporting Information Figure S4). After MTC removal, rNOE follows a slow and gradual buildup of saturation, independently of the B_1 amplitude applied. The amide pool, although also slow exchanging, displays a more characteristic buildup in saturation when applying a B_1 of $0.99 \mu\text{T}$ and $1.99 \mu\text{T}$ (Figure 7A-D; respectively). Differences in saturation buildup curves of amides and amines were more evident with a B_1 of $3.26 \mu\text{T}/2.81 \mu\text{T}$, where for the GM a fast decay trend from the amine pool is evident (similar to simulation and phantom results). Regardless of inherent concentration differences

between GM and WM, B_1 of $0.99 \mu\text{T}$ and $2.81 \mu\text{T}/3.26 \mu\text{T}$, are observed to be sensitive for separately assessing the saturation buildup of slow- and fast-exchanging components, respectively. Instead of keeping the B_1 amplitude per pulse the same, when a fixed B_1 average power was used for all mixing times, the VDMP curves were also dominated by the MTC (Supporting Information Figures S5 and S6). After removing MTC, the saturation of the pools could be observed, especially for the amide pool. However, the rNOE pool showed a less-efficient saturation and a reduced buildup when a fixed B_1 average power of $1.55 \mu\text{T}$ was used for each mixing time. Because of the

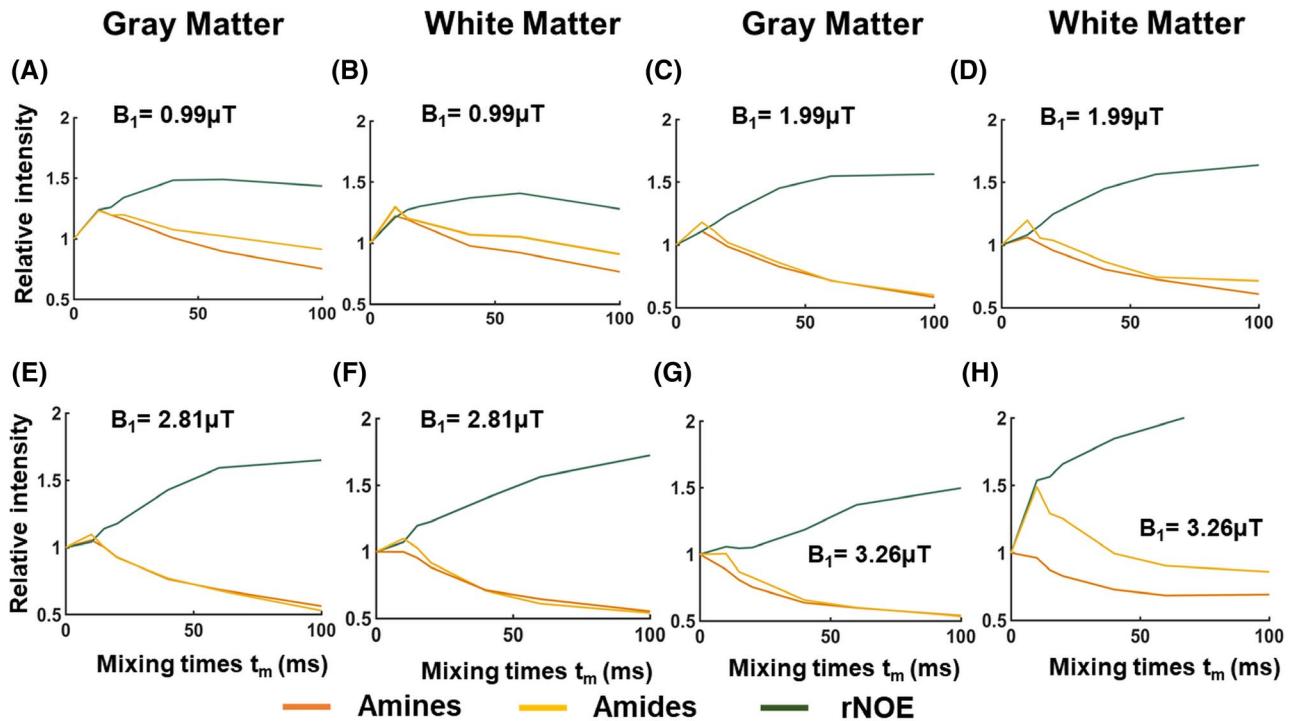


FIGURE 7 Normalized and magnetization transfer removed VDMP saturation buildup curves for different mixing times, when the B_1 amplitude applied was $0.99 \mu\text{T}$ (A,B), $1.99 \mu\text{T}$ (C,D), $2.81 \mu\text{T}$ (E,F), and $3.26 \mu\text{T}$ (G,H), from gray and white matter, respectively. rNOE, Relayed nuclear Overhauser enhancement

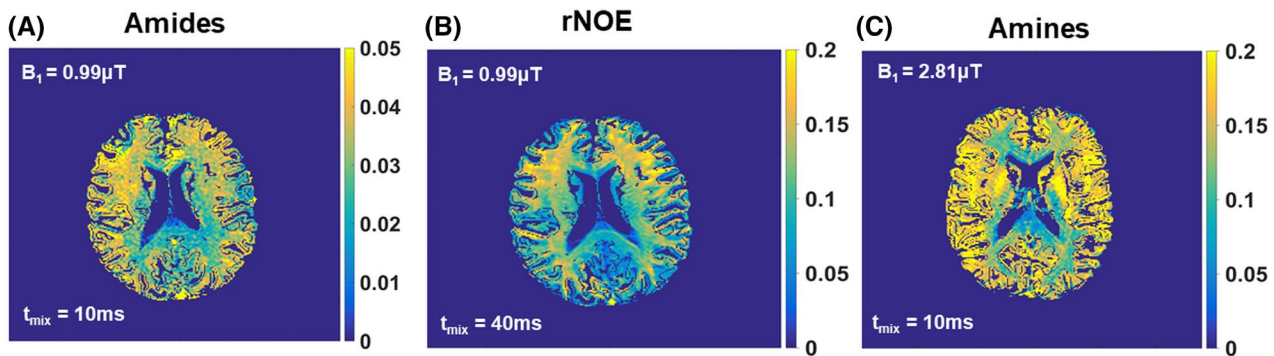


FIGURE 8 Voxel-based variable-delay multipulse maps obtained using the optimal B_1 amplitude and mixing time (t_{mix}) where the most CEST effect is observed according to the saturation buildup curves, specifically for (A) amides at 3.5 ppm, (B) rNOE at -3.5 ppm, and (C) amines at 2 ppm. rNOE, Relayed nuclear Overhauser enhancement

SAR restrictions, a B_1 average power scheme higher than $1.55 \mu\text{T}$ could not be used to acquire and observe buildup trends.

Based on VDMP buildup curves, the optimal B_1 and mixing time combinations were determined to be $0.99 \mu\text{T}$ and a t_{mix} of 10 ms and 40 ms for amide and rNOE pools, respectively. The optimal B_1 amplitude and mixing time to effectively saturate fast-exchanging amine pools were $2.81 \mu\text{T}/3.26 \mu\text{T}$ and 10/0 ms. Voxel-based VDMP maps corresponding to these B_1 and mixing times are shown in Figure 8. For the B_1 of $0.99 \mu\text{T}$, the CEST effect from amides

follows the same trend on the VDMP map (Supporting Information Figure S7) as the one observed in the buildup curves (Figure 7A): a higher CEST effect at $t_{\text{mix}} = 10$ ms followed by a decreasing CEST effect at t_{mix} of 40 ms and 100 ms. Similarly for the rNOE pool, the highest CEST effect is at $t_{\text{mix}} = 40$ ms with a B_1 of $0.99 \mu\text{T}$, in line with the VDMP buildup curves. For the fast exchanging amines, the highest CEST effect is found at $t_{\text{mix}} = 10$ ms and 0 ms for a B_1 of 2.81 and $3.26 \mu\text{T}$, respectively, as expected from the peak in saturation observed in the saturation buildup curves (Figure 8 and Supporting Information Figure S8).

The mean signal intensity values ($1 - S/S_0$) for all the GM and WM voxels are reported in Supporting Information Table S3.

4 | DISCUSSION

The aim of this study was to evaluate the potential of VDMP-CEST to assess *in vivo* proteins and metabolites in the human brain at 7T. The most salient finding of this study is the importance of removing MTC for *in vivo* VDMP applications in the human brain. By mitigating the MTC, the saturation buildup curves from amide, rNOE, and amine pools were shown for the first time from the human brain. Additionally, the influence of B_1 amplitude on the saturation efficiency was shown for different pools, suggesting the necessity to choose an optimal B_1 to separately evaluate slow- from fast-exchanging pools based on their VDMP saturation buildup curves. Finally, the optimal mixing time and B_1 combinations were reported for amide, rNOE, and amine pools in the human GM and WM.

Although VDMP-CEST is selective for fast- and slow-exchanging pools, the application *in vivo* suffers from an evident contribution from MTC (Figure 6).²⁰ Mitigating the MTC through Lorentzian fittings revealed the importance of MT removal when applying VDMP-CEST in the human brain. A previous study, aimed to suppress MT contrast, employed the subtraction of two images obtained with different mixing times.²¹ An advantage of this subtraction method is that it is easily implemented. However, because of differences in molecular composition between different tissue compartments, different levels of MTC are expected for different voxels. Moreover, in diseased tissue, pathological processes yield to changes in MTC.²⁰ This makes it difficult—if not impossible—to choose the two mixing times that would, after subtraction, eliminate the MT effect effectively within the whole image.¹¹ A more recent study in mouse brain has used a model to fit VDMP buildup curves to extract the slow- and fast-exchanging MTC components. Because relatively high B_1 peak values (6 and 12 μT) and large frequency offset ranges were used in this study, translating this approach into *in vivo* human studies would be complicated based on SAR constraints. Moreover, fitting slow-exchanging pool from VDMP curves makes it difficult to distinguish the slow MTC component from the other slow-exchanging pools such as amide and rNOE. Therefore, we proposed an alternative method, using a three-pool Lorentzian fit, which mitigates the MTC in the human GM and WM for each mixing time separately. This method was also extended to eliminate MTC on a voxel-by-voxel basis (Figure 8). Our results, in Figures 6 and 7, show that MTC removal with this

method has a considerable impact on the VDMP buildup curve trends, making it possible to observe distinguishable buildup curves from amide, rNOE, and amine pools.

Besides contributing to the MTC effect in the human brain, the B_1 amplitude of the applied RF pulses also has an impact on the saturation efficiency of the CEST pool of interest.²⁰ To determine the ideal B_1 amplitude and saturation duration, Khlebnikov et al used Bloch-McConnell equation simulations and showed that slow-exchanging (16-30 Hz) amides required a lower B_1 (<1.5 μT) and a longer saturation duration (>2.5 s).⁵ Fast-exchanging amines, such as Glu (exchange rate of ~5500 Hz), required higher B_1 (~6 μT) and shorter saturation duration (<1 s) to achieve the maximum CEST effect.⁵ Translating these parameters to the human *in vivo* situation is challenging given the maximum allowed power and SAR limitations of human MRI scanners. We investigated the optimum B_1 for most efficiently detecting amide, rNOE, and amine. When studying the B_1 effect in controlled phantom experiments (Figure 4), we could observe that slower exchanging components (amides and rNOE) are more efficiently saturated when a lower B_1 is applied and hence leading to clear buildup trends for these pools without the contribution from fast-exchanging ones. In contrast, the fast-exchanging (amine CEST) pools could be observed mainly when using a higher B_1 (3 μT). Given the presence of protein amine CEST contrast in BSA, the exchanging components in this phantom cannot be exclusively attributed to rNOE and amide proton transfer. Rather, these are thought to be derived from amide CEST, aromatic NOE, and protein amine CEST.²² In our results from the human brain (Figures 7 and 8), we could observe that for both in the GM and WM, amides and rNOE were more efficiently saturated with a B_1 amplitude of 1 μT , similar to previous simulations results.³ This is also in line with previous *in vivo* CEST studies that focused on the slow-exchanging pools such as amide and rNOE in the human brain and brain tumors at 7T.²³⁻²⁵ For rNOE, an efficient saturation was achieved independently of the B_1 amplitude used. However, with a B_1 amplitude of 1 μT , the buildup trend reached a maximum value relatively earlier before the decay starts, eliminating the need to use very long mixing times, whereas amines were more efficiently saturated with a higher B_1 amplitude of around 2.81 μT /3.26 μT .²⁶

In heterogeneous tissue, where multiple solute pools are overlapping on their resonance frequency, the effect of the interpulse delay and B_1 amplitude could be used together to modulate the effect from different pools. We evaluated the optimal combination of B_1 amplitude and t_{mix} to achieve the most sensitive saturation buildup for different CEST pools present in the human brain. Our results (Figures 7 and 8) suggest that B_1 amplitude of 1 μT and t_{mix} of 10 ms and 40 ms are optimal to achieve the

highest signal from amides and rNOE, respectively. This is in line with the slower exchanging nature of these pools. Contrary to slow-exchanging components, which need a low B_1 amplitude and longer interpulse delays, high B_1 amplitude in combination with a short interpulse delay is needed to detect signal from fast-exchanging components because of their rapid saturation. The highest signal from amines were found using a B_1 amplitude of 2.81 μT /3.26 μT and with a combination of a very short ($t_{\text{mix}} = 10$ ms) or no interpulse delay ($t_{\text{mix}} = 0$ ms). The short time necessary to achieve maximum saturation highlights the fast-exchanging nature of amines, which is in accordance with previous studies from the human brain.²⁶ A previous study explored VDMP for quantification of fast-exchanging metabolites.¹⁰ In agreement with our results, it was shown that Glu's signal in a phantom predominantly decayed for increasing mixing times.¹⁰ By using these optimal values, the CEST contrast observed on the voxel-based VDMP maps from amides, rNOE, and amines (Figure 8) were in accordance with the GM/WM distribution of the corresponding solutes, as well as the CEST effects observed from these molecules in GM and WM in previous work.²⁷⁻³⁰

Based on the voxel-based maps (data not shown), it is, however, not possible to specifically distinguish Glu that resonates at around 3 ppm from other possible amine groups (that resonate at around 2 ppm). For instance, creatine (amine group at 2 ppm) has a slightly slower exchange rate (810 Hz) than that of Glu (5500 Hz). However, the overlap of both pools in the frequency spectra makes separation too challenging,³¹ whereas the saturation buildup curves of amines overlapped with those of amides at 3.5 ppm at lower B_1 amplitudes (<2.81 μT), contrary to what is observed at higher amplitudes ($B_1 = 2.81$ μT and 3.26 μT ; Figure 7). This suggests that fast-exchanging molecules were simply not observable at these lower B_1 amplitudes. Thus, when applying VDMP, the choice of B_1 can help in differentiating slow- and fast-exchanging pools. Slight differences between the voxel-based maps and the VDMP-curves might be explained by the fact that the later results from the average signal observed in the GM and WM.

The simulations and phantom results (Figures 3 and 4) aimed to illustrate how VDMP buildup curves would display the saturation buildup of the CEST pools of interest in ideal conditions. In the present investigation, we could show how our *in vivo* data are—to a certain extent—in line with these results (Figures 3 and 4 vs Figures 6 and 7). Different factors derived from the heterogeneous nature of human brain tissue such as T_1 relaxation, MTC, and the eventual interplay between different compounds, play a role in the underlying CEST signal observed in our *in vivo* results.

Our study has some limitations. Our VDMP simulations did not consider the B_1 amplitude of the RF pulse.

Therefore, simulation results are limited to show the effect of the number of VDMP pulses and duration, as well as the saturation buildup of the CEST pools of interest. Moreover, when calculating the Z-magnetization as an average of the imaged voxels, the quality of calculated CEST signal can be affected by the number of voxels included. Voxel-based VDMP maps were therefore investigated and corroborated the findings from the ROI-based results. Additionally, the number of VDMP pulses and their duration were kept constant for this study. Xu et al have shown through simulations that for a B_1 of 4 μT , the most efficient saturation buildup could be reached when using 16 to 32 pulses.⁶ Therefore, the number and amplitude of RF pulses were chosen accordingly to achieve a sufficient saturation within SAR limits and a feasible scanning time on a human 7T MRI scanner. It would be interesting to investigate the relationship between the pulse duration and number, as well as B_1 amplitude, to better target specific CEST pools *in vivo* of the human brain at 7T. We also maintained the B_1 amplitude constant for each pulse, which results in a decrease of the B_1 average power with an increased interpulse delay. In one volunteer (Supporting Information Figures S5 and S6), we kept the B_1 average power constant for the entire saturation duration to investigate the effect of fixed B_1 average power. With the fixed B_1 average power, we observed a similar VDMP buildup trend for amines and amides, impairing pool differentiation (possibly caused by the use of low B_1 amplitude for shorter t_{mix}). This suggests that for overall saturation efficiency it is more valuable to fix the B_1 amplitude per pulse, independently from the mixing time. The T_2 of the evaluated pools were mostly longer than the pulse duration used (amide 100 ms, amine 200 ms, and rNOE 5 ms).²⁰ Therefore, the T_2 relaxation during the pulse is not expected to affect water protons for amide and amine pools, also in line with the previous explanation on how the VDMP pulses could serve as a T_2 filter.⁶ rNOE effects, however, are more complex and of a relayed nature. Further work is needed to investigate the influence of T_1 and the T_2 relaxation on the VDMP saturation buildup trends for these pools, as well as quantifying the contribution of slow- and fast-exchanging components, including multiple existent exchange rates per CEST pool. For instance, amine protons were also reported to be present in proteins, and were shown to contribute to amineCEST contrast in the rat brain.³¹ In our study, we were not able to differentiate between the amineCEST contrast deriving from metabolites such as Glu and the ones from proteins. Finally, model-based fitting with predefined boundary values is a limitation, especially when a short frequency-offset range is used. The fittings were adequate for MTC removal; however, additional work is necessary to verify this method further *in vivo* and in pathology.

5 | CONCLUSION

VDMP-CEST relies on the inherent differences in exchange rates of slow- and fast-exchanging solute pools. We have proposed a new method to mitigate the MTC effect in VDMP-CEST. By mitigating the MTC through Lorentzian fittings and using the mixing time as an exchange filter, we obtained the saturation buildup curves from amide, rNOE, and amine pools for the first time from the human brain. The MTC removal is essential to distinguish solute pools with different exchange rates from the human brain *in vivo*. Moreover, the mixing time and maximum RF amplitude (B_1) should be carefully chosen to increase the specificity to the solute pool of interest. Our results suggest that VDMP has potential to mitigate the challenge to separately evaluate fast- and slow-exchanging CEST-pools in the human brain *in vivo*.

ACKNOWLEDGMENTS

This study is part of the project “Non-Invasive Characterization of Active Multiple Sclerosis Lesions Through Chemical Exchange Saturation Transfer (CEST) Imaging” (project no. 16862) financed by the Dutch Research Council (NWO) Talent Programme Veni. This work was also funded by the Medical Delta Cancer Diagnostics 3.0 program.

ORCID

Bárbara Schmitz-Abecassis  <https://orcid.org/0000-0003-1776-4560>

Elena Vinogradov  <https://orcid.org/0000-0003-4607-4147>


Jannie P. Wijnen  <https://orcid.org/0000-0003-2352-3667>

Thijs van Harten  <https://orcid.org/0000-0002-3408-9379>

Evita C. Wieggers  <https://orcid.org/0000-0001-5451-2990>

Hans Hoogduin  <https://orcid.org/0000-0001-7707-0750>

Matthias J. P. van Osch  <https://orcid.org/0000-0001-7034-8959>

Ece Ercan  <https://orcid.org/0000-0002-8187-2075>

TWITTER

Ece Ercan  @aeceercan

REFERENCES

1. Van Zijl PCM, Yadav NN. Chemical exchange saturation transfer (CEST): what is in a name and what isn't? *Magn Reson Med*. 2011;65:927-948.
2. Dou W, Lin C-Y, Ding H, et al. Chemical exchange saturation transfer magnetic resonance imaging and its main and potential applications in pre-clinical and clinical studies. *Quant Imaging Med Surg*. 2019;9:1747-1766.
3. Khlebnikov V, van der Kemp WJM, Hoogduin H, Klomp DWJ, Prompers JJ. Analysis of chemical exchange saturation transfer contributions from brain metabolites to the Z-spectra at various field strengths and pH. *Sci Rep*. 2019;9:1-11.
4. Zhou J. Amide proton transfer imaging of the human brain. *Methods Mol Biol*. 2011;711:227-237.
5. Xu X, Yadav NN, Zeng H, et al. Magnetization transfer contrast-suppressed imaging of amide proton transfer and relayed nuclear Overhauser enhancement chemical exchange saturation transfer effects in the human brain at 7T. *Magn Reson Med*. 2016;75:88-96.
6. Xu J, Yadav NN, Bar-Shir A, et al. Variable delay multi-pulse train for fast chemical exchange saturation transfer and relayed-nuclear overhauser enhancement MRI. *Magn Reson Med*. 2014;71:1798-1812.
7. Haris M, Nanga RPR, Singh A, et al. Exchange rates of creatine kinase metabolites: feasibility of imaging creatine by chemical exchange saturation transfer MRI. *NMR Biomed*. 2012;25:1305-1309.
8. Zhou J, Payen JF, Wilson DA, Traystman RJ, Van Zijl PCM. Using the amide proton signals of intracellular proteins and peptides to detect pH effects in MRI. *Nat Med*. 2003;9:1085-1090.
9. Heo HY, Han Z, Jiang S, Schär M, van Zijl PCM, Zhou J. Quantifying amide proton exchange rate and concentration in chemical exchange saturation transfer imaging of the human brain. *Neuroimage*. 2019;189:202-213.
10. Xu J, Chan KWY, Xu X, Yadav N, Liu G, Van Zijl PCM. On-resonance variable delay multi pulse scheme for imaging of fast-exchanging protons and semi-solid macromolecules HHS public access. *Magn Reson Med*. 2017;77:730-739.
11. Chen L, Xu X, Zeng H, et al. Separating fast and slow exchange transfer and magnetization transfer using off-resonance variable-delay multiple-pulse (VDMP) MRI. *Magn Reson Med*. 2018;80:1568-1576.
12. Dortch RD, Moore J, Li KE, et al. Quantitative magnetization transfer imaging of human brain at 7 T. *NeuroImage*. 2013;64:640-649.
13. Nehrke K, Börner P. DREAM-a novel approach for robust, ultrafast, multislice B1 mapping. *Magn Reson Med*. 2012;68:1517-1526.
14. Lin EC, Li H, Zu Z, et al. Chemical exchange rotation transfer (CERT) on human brain at 3 Tesla. *Magn Reson Med*. 2018;80:2609-2617.
15. Jenkinson M, Beckmann CF, Behrens TEJ, Woolrich MW, Smith SM. Fsl. *Neuroimage*. 2012;62:782-790.
16. Smith SM. Fast robust automated brain extraction. *Hum Brain Mapp*. 2002;17:143-155.
17. Zhang Y, Brady M, Smith S. Segmentation of brain MR images through a hidden Markov random field model and the expectation-maximization algorithm. *IEEE Trans Med Imaging*. 2001;20:45-57.
18. Reuter M, Schmansky NJ, Rosas HD, Fischl B. Within-subject template estimation for unbiased longitudinal image analysis. *Neuroimage*. 2012;61:1402-1418.
19. Windschuh J, Zaiss M, Meissner J-E, et al. Correction of B1-inhomogeneities for relaxation-compensated CEST imaging at 7T. *NMR Biomed*. 2015;28:529-537.
20. van Zijl PCM, Lam WW, Xu J, Knutsson L, Stanisz GJ. Magnetization transfer contrast and chemical exchange saturation transfer MRI. Features and analysis of the field-dependent saturation spectrum. *Neuroimage*. 2018;168:222-241.
21. Shu Z, Xu Y, Shao Y, Pang P, Gong X. Radiomics from magnetic resonance imaging may be used to predict the progression of white matter hyperintensities and identify associated risk factors. *Eur Radiol*. 2020;30:3046-3058.

22. Lee JS, Xia D, Jerschow A, Regatte RR. In vitro study of endogenous CEST agents at 3T and 7T. *Contrast Media Mol Imaging*. 2016;11:4-14.
23. Jones CK, Huang A, Xu J, et al. Nuclear Overhauser enhancement (NOE) imaging in the human brain at 7T. *Neuroimage*. 2013;77:114-124.
24. Khlebnikov V, Polders D, Hendrikse J, et al. Amide proton transfer (APT) imaging of brain tumors at 7T: the role of tissue water T1-relaxation properties. *Magn Reson Med*. 2017;77:1525-1532.
25. Zaiss M, Windschuh J, Paech D, et al. Relaxation-compensated CEST-MRI of the human brain at 7T: unbiased insight into NOE and amide signal changes in human glioblastoma. *Neuroimage*. 2015;112:180-188.
26. Cai K, Haris M, Singh A, et al. Magnetic resonance imaging of glutamate. *Nat Med*. 2012;18:302-306.
27. Singh A, Debnath A, Cai K, et al. Evaluating the feasibility of creatine-weighted CEST MRI in human brain at 7 T using a Z-spectral fitting approach. *NMR Biomed*. 2019;32.
28. Jones CK, Huang A, Xu J, et al. Nuclear Overhauser enhancement (NOE) imaging in the human brain at 7T. *Neuroimage*. 2013;77:114-124.
29. Cai K, Singh A, Roalf DR, et al. Mapping glutamate in subcortical brain structures using high-resolution GluCEST MRI. *NMR Biomed*. 2013;26:1278-1284.
30. Khlebnikov V, Windschuh J, Siero JCW, et al. On the transmit field inhomogeneity correction of relaxation-compensated amide and NOE CEST effects at 7 T. *NMR Biomed*. 2017;30:1-10.
31. Cui J, Zu Z. Towards the molecular origin of glutamate CEST (GluCEST) imaging in rat brain. *Magn Reson Med*. 2020;83:1405-1417.

SUPPORTING INFORMATION

Additional Supporting Information may be found online in the Supporting Information section.

FIGURE S1 B_1 maps from the human brain, corresponding to volunteers scanned with different B_1 amplitudes: using a B_1 amplitude of 0.99 μT (A), 2.81 μT (B), 1.99 μT (C), 3.26 μT (D) and a fixed B_1 average power of 1.55 μT (E)

FIGURE S2 Region of interest (in white) overlaid on the CEST image from the phantom, for all different vials: (1) Glutamate, (2) Egg White (data not shown), (3) Mixture of glutamate and BSA 10% and (4) BSA 10%

FIGURE S3 Histograms of the fitting parameters and corresponding number of voxels for gray and white matter respectively. The fitting parameters obtained using a larger

frequency offset range ($-75\,000\text{ Hz}$ to $750\,000\text{ Hz}$) is compared with those obtained with a shorter frequency range (-1500 Hz to 1500 Hz)

FIGURE S4 Average VDMP saturation buildup curves from all voxels included, and corresponding standard deviation, for different mixing times, when the B_1 amplitude applied was 0.99 μT (A and B), 1.99 μT (C and D), 2.81 μT (E and F), and 3.26 μT (G and H), from gray (GM) and white matter (WM), respectively

FIGURE S5 Z-spectra from *in vivo* human gray and white matter when scanning with a fixed B_1 average power of 1.55 μT

FIGURE S6 VDMP build-curves from *in vivo* human gray and white matter when scanning with a fixed B_1 average power of 1.55 μT . In the upper row the magnetization transfer contrast is still present and in the lower row it has been removed

FIGURE S7 B_1 corrected VDMP-CEST maps of the *in vivo* human gray and white matter from four different mixing times (t_{mix}) and acquired with the optimal B_1 amplitude, which results in the most efficient saturation for the CEST pool of interest

FIGURE S8 B_1 corrected VDMP-CEST maps of Amines contrast in the *in vivo* human gray and white matter of mixing times (t_{mix}) 10 ms at: A) $B_1 = 2.81\ \mu\text{T}$ and mixing times (t_{mix}) 0 ms, B) $B_1 = 2.81\ \mu\text{T}$ and t_{mix} 10 ms, C) $B_1 = 3.26\ \mu\text{T}$ and t_{mix} 0 ms & D) $B_1 = 3.26\ \mu\text{T}$ and t_{mix} 10 ms

TABLE S1 B_1 amplitudes used to acquire *in vivo* human brain VDMP-CEST images and the corresponding B_1 average power values for different mixing times

TABLE S2 Parameters used for Lorentzian fittings

TABLE S3 Mean $1-S/S_0$ values from the gray matter and white matter voxels are reported for amide, rNOE and amines pool when using the most optimal B_1 and mixing time for each CEST pool detection

How to cite this article: Schmitz-Abecassis B, Vinogradov E, Wijnen JP, et al. The use of variable delay multipulse chemical exchange saturation transfer for separately assessing different CEST pools in the human brain at 7T. *Magn Reson Med*. 2022;87:872-883. <https://doi.org/10.1002/mrm.29005>